PHYSICAL REVIEW E **81**, 041704 (2010)

Molecular dynamics simulations of the liquid-crystal phases of 2-(4-butyloxyphenyl)-5-octyloxypyrimidine and 5-(4-butyloxyphenyl)-2-octyloxypyrimidine

R. Pecheanu and N. M. Cann[*]

Department of Chemistry, Queen's University, Kingston, Ontario, Canada K7L 3N6

(Received 24 November 2009; published 30 April 2010)

In this paper, molecular dynamics simulations are employed to study the liquid-crystal phases of 2-(4-butyloxyphenyl)-5-octyloxypyrimidine and 5-(4-butyloxyphenyl)-2-octyloxypyrimidine. Both mesogens consist of aromatic phenyl-pyrimidine cores in between two identical alkoxy tails, but they differ in the preferred core conformation. The *ab initio*–based derivation of suitable molecular models is discussed in detail, with particular emphasis on capturing proper ring-ring interactions. The presence of ring quadrupoles in the molecular model is shown to be essential to the correct reproduction of the experimentally observed phases. Simulations of these fluids at various temperatures are performed and order, for the aromatic core and the flexible tails, is analyzed. To differentiate smectic-*A* from smectic-*C* phases, intermolecular structure is divided into contributions parallel and perpendicular to the director and layer normal.

DOI: 10.1103/PhysRevE.81.041704　　　PACS number(s): 61.30.Cz, 61.30.Pq, 61.20.Ja

I. INTRODUCTION

Liquid crystals, by virtue of being intermediate between isotropic liquids and crystalline solids, display a range of unique properties. Their practical uses, most notably for displays on cellular phones, televisions, watches, computers, cameras, and video recorders, are well known [1–3]. Chiral smectic-*C* (Sm-*C*) liquid crystals exhibit ferroelectric properties and, for this reason, hold considerable promise for application purposes [4,5]. In most cases, chiral smectic phases are produced by the addition of a small amount of a chiral dopant to an achiral host. Systematic experimental studies have been undertaken [6–8] to correlate host and dopant characteristics with the pitch and polarization of the phase. Multiple mechanisms for the chirality transfer have been proposed [7,9,10] based on experimental results. However, theoretical studies have been restricted to predictions based on the attributes of the chiral additive alone [11–14]. While these studies have yielded important insights into the dopant impact, by design they cannot provide detailed molecular information on the mechanism of dopant-to-host chirality transfer. As a first step, the characteristics of the hosts and their phases must be understood. To this end, a comprehensive study of 2-(4-butyloxyphenyl)-5-octyloxypyrimidine (2PhP), a well-known liquid-crystal host [15–21], is carried out in this paper. A similar mesogen, 5-(4-butyloxyphenyl)-2-octyloxypyrimidine (5PhP), which differs from 2PhP only in the molecular core, is also examined. 5PhP has not been studied as a host but it has been employed as a cohost for 2PhP where it enhanced the electroclinic coefficient [22,23] in chiral smectic-*A* (Sm-*A*) phases and the polarization power of the smectic-*C* phase [24]. The experimental phase diagram of 2PhP is characterized by the presence of a Sm-*C* phase extending from 58 to 85 °C whereas 5PhP only shows a Sm-*A* phase. The structures of 2PhP and 5PhP, and their experimental phase diagrams, are provided in Fig. 1.

Molecular-dynamics (MD) simulations have provided important details on intermolecular structure and orientational order for many liquid crystalline phases. Typical simulations employ simple models, such as multipolar ellipsoids [25,26], cylinders [27,28], or fused ellipsoids or cylinders [29,30]. Despite their simplicity, many of these models display a rich phase structure. The Sm-*C* phase, however, has proved elusive [31] for many of these models. In 1998,

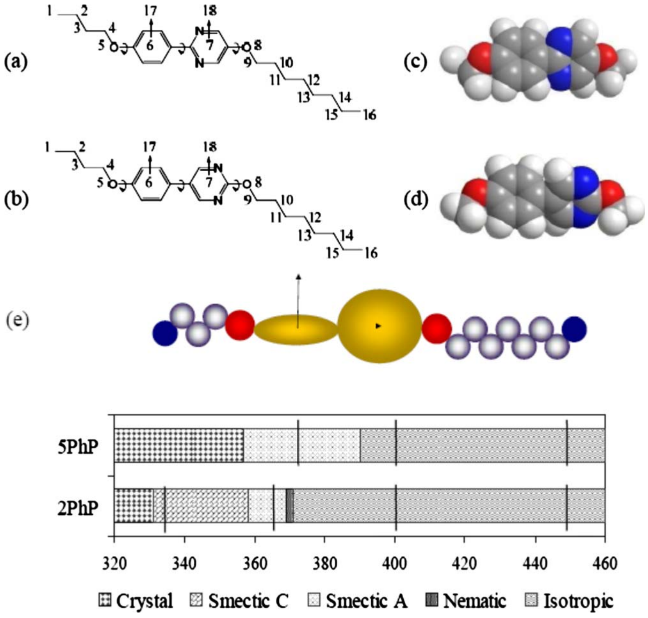

FIG. 1. (Color online) 2PhP and 5PhP models and phase diagrams. (a) Structure of 2-(4-butyloxyphenyl)-5-octyloxypyrimidine (2PhP). (b) Structure of 5-(4-butyloxyphenyl)-2-octyloxypyrimidine (5PhP). (c) Snapshot of *ab initio* optimized core of the 2PhP molecule. (d) Snapshot of *ab initio* optimized core of the 5PhP molecule. (e) Schematic multisite coarse-grained representation of the 2PhP and 5PhP liquid-crystal molecules. The aromatic units, oxygen atoms, methylene groups, and methyl groups are shown in yellow, red, gray, and blue, respectively. (f) Phase sequences [24] of 2PhP and 5PhP. Vertical bars show the temperature at which the MD simulations have been run.

---

[*] Author to whom correspondence should be addressed. FAX: 613-533-6669; ncann@chem.queensu.ca

Neal and Parker [31] found that the introduction of a longitudinal quadrupole to an ellipsoidal molecular model produced Sm-*C* phases. Quadrupoles are also of interest in this work and we explore their impact for the aromatic rings of 2PhP and 5PhP. The feasibility of more realistic molecular models has been discussed by Zannoni *et al.* [32]. The progression from simple models to complex ones is challenging for several reasons: the computational cost increases for a more sophisticated molecular representation, many molecules are required in the simulation cell to properly model the phase structure, and longer simulations (tens of nanoseconds) are needed as the dynamics slow down due to molecular entanglement. Despite these challenges, many mesogens require accurate molecular models to capture their phase behavior. A comparison between 2PhP and 5PhP, for example, requires detailed molecular representations since their structures are very similar. To this end, we have developed semi-coarse-grained models, where the aromatic rings are represented by soft quadrupolar ellipsoids, but the chains are given an atomistic representation. In order to fully analyze the impact of the core representation, four ring models are explored for each mesogen. *Ab initio* calculations are employed to properly explore the energetic costs for bends and torsions, and these are used in the development of the molecular models. The inclusion of quadrupoles complicates and lengthens the simulations, but proper ring-ring interactions are necessary to correctly represent core-core interactions between neighboring molecules. All-atom force fields appear to provide a superior alternative to our chosen models for 2PhP and 5PhP, however, these models do not properly account for the quadrupole that arises from the electron clouds above and below the plane of the ring. We show, by a detailed exploration of pair interaction energies, that the quadrupolar ring model leads to a crucial energetically favorable crossed-core conformation that impacts the phases of 2PhP and 5PhP. We have also found that the proper representation of the phenyl-pyrimidine torsion within the molecular core is essential to the phase difference between 2PhP and 5PhP.

With suitable molecular models in hand, detailed molecular dynamics simulations of 2PhP and 5PhP are conducted to examine the smectic phases. We consider several order parameters, some defined by the molecular cores and others obtained for the alkoxy tails. The layer normal and associated order parameter are also evaluated. Intermolecular structure is analyzed via the decomposition of pair distributions parallel or perpendicular to the director and the layer normal. A comparison of these distributions differentiates Sm-*C* from Sm-*A* and reveals layer spacing as a function of temperature. Orientational distributions are also evaluated and show the relative positions of neighboring molecules. We find that the molecular cores are ordered but the alkoxy tails are fluid and their distribution is liquidlike. 2PhP is examined at four temperatures (335, 365, 400, and 450 K) to span the temperature range from Sm-*C* to isotropic. Simulations of 5PhP are conducted at 370, 400, and 450 K.

Section II describes the model development, particularly the steps implemented to arrive at a suitable representation of the ring potentials. Simulation details are provided in Sec. III. The ordered phases of 2PhP and 5PhP are examined in Sec. IV. Concluding remarks are presented in Sec. V.

II. 2PHP AND 5PHP MOLECULAR MODELS

The structures of 2PhP and 5PhP are provided in Figs. 1(a) and 1(b), respectively. The molecular cores consist of joined pyrimidine and phenyl rings, and beyond the core, oxygen atoms connect to flexible hydrocarbon chains. 2PhP and 5PhP differ only in the connection point between the phenyl and pyrimidine rings.

In order to efficiently represent 2PhP and 5PhP, a semi-coarse-grained model is adopted for the rings, as shown in Fig. 1(e). Note from the figure that the phenyl and pyrimidine rings are individually represented as soft ellipsoids. The rings may bear a partial charge and a quadrupole perpendicular to the ring plane. The latter is reflective of the π charge cloud above and below the ring. Molecular flexibility is also crucial to the representation of these mesogens. Torsional motion within the models is fully represented, including the phenyl-pyrimidine torsion and the flexibility of the alkoxy tails.

Full details of the 2PhP and 5PhP model development are provided in this section. First, *ab initio* studies of 2PhP and 5PhP yield intramolecular potentials and atomic charges. Second, a careful procedure for the development of the ring models, starting with comparisons to *ab initio* pair potentials for benzene dimers [33,34], is undertaken.

A. *Ab initio* calculations for 2PhP and 5PhP

A comprehensive series of *ab initio* geometry optimizations [35] have been performed, at the B3LYP/6-311++$G(d,p)$ level of theory [36–38], to examine the structure and flexibility of 2PhP and 5PhP. Since the molecules are large and the terminal alkyl chains are well represented by standard potentials, methoxy groups replace the chains as shown in Figs. 1(c) and 1(d). Initially, full geometry optimizations were performed to ascertain the minimum-energy conformation and to obtain partial atomic charges. The CHELPG (charges from electrostatic potentials using a grid) algorithm [39] was adopted for the charges and results are available in Table S1 of the supplemental materials [40]. Atomic charges for the omitted part of the alkoxy chains were set to zero, as these are methyl and methylene sites that typically do not bear significant charge. Energetic costs associated with molecular flexibility were evaluated from *ab initio* calculations in which one angle was constrained while the rest of the molecular structure was allowed to relax. We considered only bends and torsions for 2PhP and 5PhP, with the bond lengths kept fixed using the RATTLE algorithm [41]. The equilibrium bond lengths were extracted from the minimum-energy structure and are listed in Table S2 of the supplemental materials [40].

The energy required to bend is represented by a harmonic potential

$$U_{bending}(\theta) = k(\theta - \theta_0)^2, \tag{1}$$

where k, θ, and θ_0 are the force constant, the angle, and the equilibrium angle, respectively. The equilibrium angles are obtained from the minimum-energy structure. The corresponding force constants are obtained from a least-squares fit to 11 restricted geometry optimizations, where the angle of

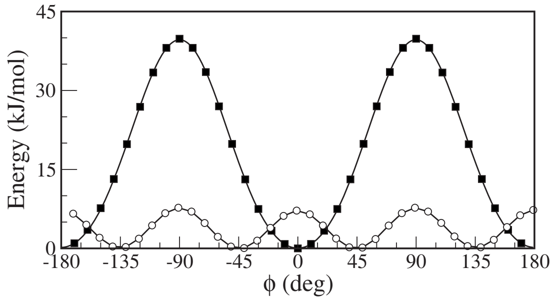

FIG. 2. Phenyl-pyrimidine torsional energy as a function of the ring-ring torsion angle for 2PhP (filled squares) and 5PhP (open circles). Solid lines show the fitted torsional potentials [see Eq. (2)].

interest is given a value within $\theta_0 \pm 5^0$. Bending potentials are calculated for both alkoxy oxygens (see Table S3 of the supplemental materials [40]). Within the ring regions, bending potentials are introduced to preserve linearity along the O(5)-phenyl(6)-pyrimidine(7)-O(8) axis (see Fig. 1 for numbering). Since the ring atoms are not explicitly included in the potential, the ring is represented by its center and by a "ghost" site placed on the vector normal to the ring plane. These "ghost atoms" are identified as sites "17" and "18" in Figs. 1(a) and 1(b). Bending distortions of the ring can be represented via these two points, as shown in the supplemental materials [40], and we have included potentials for bending at a ring. For instance, an O(5)-phenyl(6)-pyrimidine(7) potential accounts for the energetic cost of a bend at the phenyl(6) ring. Likewise, a ghost(17)-phenyl(6)-O(5) bend potential provides an energetic cost for out-of-plane torsion of the ring.

Torsional motion is represented by a Ryckaert-Bellemans [42] type potential

$$U_{torsion}(\phi) = \sum_{n=0}^{6} c_n \cos^n \phi, \tag{2}$$

where c_n is the coefficient of the ith term and ϕ is the dihedral angle. For each torsion, 18–36 restricted geometry optimizations are performed with the selected dihedral angle fixed. Torsional potentials have been calculated for twisting motions involving one or both rings. Specifically, the energetic costs for twisting about the bond joining an oxygen to a ring carbon have been assessed, along with the phenyl-pyrimidine twist. Inter-ring π conjugation is maximized for a planar arrangement but steric considerations lead to important differences between 2PhP and 5PhP. Figure 2 compares the phenyl-pyrimidine torsion potentials for 2PhP and 5PhP. The former strongly favors planarity between the rings but the latter prefers a nonplanar ring arrangement due to steric crowding of proximal orthohydrogens. The torsion barrier is also lower for 5PhP indicating more flexibility within the core.

B. Aromatic ring models

The details of the ring models are expected to be highly relevant to the proper description of 2PhP and 5PhP. Our goal is to arrive at a practical, realistic representation of the mesogenic cores. Several coarse-grained representations for biphenyl, cyanobiphenyl, and longer *p*-phenyls have been employed by others [43–45], but the rings are collectively represented by a single elongated ellipsoid. The requirement for a ring quadrupole and a phenyl-pyrimidine torsion cannot be accomplished with this approach. At a minimum, each ring must be individually represented. Cross and Fung [46] represented the individual rings in their model for 4-n-pentyl-4′-cyanobiphenyl but the rings were modeled as nonpolar spheres. Coarse-grained models for benzene have been proposed by others [47,48] and our model is similar to the quadrupolar ring model adopted by Cacelli *et al.* [48].

The phenyl and pyrimidine rings are represented by multipolar uniaxial Gay-Berne (GB) ellipsoids. Between two rings, the GB potential has the form [49]

$$U_{AB}(\hat{u}_A,\hat{u}_B,\vec{r}_{AB}) = 4\varepsilon_{AB}(\hat{u}_A,\hat{u}_B,\hat{r}_{AB})[R^{12} - R^6], \tag{3}$$

where the orientations of the two rings, A and B, are identified by unit vectors $\hat{u}_A$ and $\hat{u}_B$, respectively, that are normal to the ring plane and intersect the center of the ring. The vector joining the ring centers is $\vec{r}_{AB}$ and the corresponding unit vector is $\hat{r}_{AB}$. In this work, the rings are modeled as disks (i.e., discotic ellipsoids) and the anisotropy of ring-ring interactions is defined by parameters contained in R and $\varepsilon_{AB}(\hat{u}_A,\hat{u}_B,\hat{r}_{AB})$.

The distance-dependent ratio R, in Eq. (3), is

$$R = \frac{\xi_{AB}\sigma_{AB}^0}{r_{AB} - \sigma_{AB}(\hat{u}_A,\hat{u}_B,\hat{r}_{AB}) + \xi_{AB}\sigma_{AB}^0}, \tag{4}$$

where ξ_{AB} is a dimensionless parameter that allows for variation of the width of the potential well, independent of its depth and position. σ_{AB}^0 defines the overall size of the ring. Shape anisotropy is contained in the expression for $\sigma_{AB}(\hat{u}_A,\hat{u}_B,\hat{r}_{AB})$ provided in the Appendix.

The anisotropic well-depth parameter $\varepsilon_{AB}(\hat{u}_A,\hat{u}_B,\hat{r}_{AB})$ is a product of three terms:

$$\varepsilon_{AB}(\hat{u}_A,\hat{u}_B,\hat{r}_{AB}) = \varepsilon_{AB}^0[\varepsilon_{AB}^{(1)}(\hat{u}_A,\hat{u}_B)]^{\nu_{AB}}[\varepsilon_{AB}^{(2)}(\hat{u}_A,\hat{u}_B,\hat{r}_{AB})]^{\mu_{AB}}, \tag{5}$$

where ε_{AB}^0 defines the overall well depth, and $\varepsilon_{AB}^{(1)}(\hat{u}_A,\hat{u}_B)$ and $\varepsilon_{AB}^{(2)}(\hat{u}_A,\hat{u}_B,\hat{r}_{AB})$ introduce a dependence on molecular orientation. Expressions for $\varepsilon_{AB}^{(1)}(\hat{u}_A,\hat{u}_B)$ and $\varepsilon_{AB}^{(2)}(\hat{u}_A,\hat{u}_B,\hat{r}_{AB})$ are provided in the Appendix.

Within the simulations, identical GB parameters are used for the phenyl and pyrimidine rings. Overall, following the Appendix, nine parameters are used in the ring model: σ_{AA}^0, ε_{AA}^0, ξ_{AA}, ν_{AA}, μ_{AA}, σ_{AA}^{ee}, σ_{AA}^{ss}, ε_{AA}^{ee}, and ε_{AA}^{ss}, where the superscripts "*ee*" and "*ss*" denote end-to-end and side-by-side ellipsoids. The end-to-end and side-by-side distances, σ_{AA}^{ee} and σ_{AA}^{ss}, determine the aspect ratio of the ring. Likewise, the energy well depths for the end-to-end and side-by-side configurations determine the relative energetics of these ring arrangements.

In addition to the GB ring model, a quadrupole moment is placed along the ring axis to reflect the impact of the π charge cloud. The quadrupole-quadrupole contribution to the interaction potential is

$$U_{AB}^{QQ}(\hat{u}_A,\hat{u}_B,\vec{r}_{AB}) = \frac{3}{4}\frac{Q_A^* Q_B^*}{r_{AB}^5}[1 + 2(\hat{u}_A \cdot \hat{u}_B)^2 - 5(\hat{u}_A \cdot \hat{r}_{AB})^2 - 5(\hat{u}_B \cdot \hat{r}_{AB})^2 - 20(\hat{u}_A \cdot \hat{r}_{AB})(\hat{u}_B \cdot \hat{r}_{AB}) \times (\hat{u}_A \cdot \hat{u}_B) + 35(\hat{u}_A \cdot \hat{r}_{AB})^2(\hat{u}_B \cdot \hat{r}_{AB})^2], \quad (6)$$

where Q_A^* and Q_B^* are the reduced quadrupole moments of rings A and B, respectively.

C. Benchmarking the ring potential: Benzene and biphenyl

A systematic approach to the determination of optimal GB parameters has been undertaken. We first optimized the potential parameters for benzene, based on comparisons to *ab initio* potential-energy curves for the dimer [33,34], comparisons to experimental pair distribution functions for bulk benzene [50–54], and by comparison to the self-diffusion coefficient of bulk benzene [55–58]. We then proceeded to analyze the validity of the ring model for biphenyl.

For benzene, the intermolecular potential is written a sum of two terms, a Gay-Berne interaction and a quadrupole-quadrupole contribution

$$U = \sum_{i=1}^{N_{\text{GB}}} \sum_{j>i}^{N_{\text{GB}}} U_{ij}^{QQ} + \sum_{i=1}^{N_{\text{GB}}} \sum_{j>i}^{N_{\text{GB}}} U_{ij}^{\text{GB/GB}}. \quad (7)$$

As a start, the nine parameters of the GB potential have been least-squares fitted to reproduce *ab initio* pair energies [33,34] for 118 dimer configurations using a fixed quadrupole moment of -1.38×10^{-39} C m^2. This quadrupole is smaller than the experimental gas phase moment [59] (-2.9×10^{-39} C m^2) but is consistent with the value recommended by Cacelli *et al.* [48] for a quadrupolar benzene model. The optimal GB parameters reproduce, to very high accuracy, the *ab initio* potential-energy curves.

With this set of parameters in hand, molecular dynamics simulations in the canonical (*NVT*) ensemble for a system of 500 benzene molecules, at 300 K and a density of 0.87 g/mL, were undertaken. Although this simulation of liquid benzene yields radial distribution functions in reasonable agreement with published theoretical curves [56], a closer inspection of snapshots reveals the presence of holes in the simulation cell. Clearly, the model, although providing a very accurate representation of gas phase benzene *pairs*, does not provide a good representation for benzene *in the bulk*. We have proceeded under the assumption that the nine GB parameters are roughly correct but require adjustment to arrive at a satisfactory representation of benzene in the bulk.

Experimental carbon-carbon distributions for liquid benzene, based on extensive x-ray [54] studies, are available for comparison. To adjust each of the nine GB parameters, three values are considered: 80%, 100%, and 120% of the value obtained by optimization to *ab initio* pair potentials. Consistent with this approach, quadrupoles varying from 21% to 92% of the experimental value have also been examined. In total, 6561 parameter sets have been examined for bulk benzene. For each set, canonical MD simulations at 298 K and 0.87 g/mL have been carried out. To compare to carbon-carbon distributions from experiment, ghost atoms were placed inside the GB potential at positions consistent with the carbon atom locations in the benzene molecule and radial distributions were calculated between these sites. Least-squares errors were calculated from the comparison between the experimental carbon-carbon distribution and the distribution obtained for each parameter set. Based on this, ten models have been chosen for further consideration. These are identified as A*n*, B*n*, or C, where "*n*" is the model and A, B, and C identify that the quadrupole moment is -2.18×10^{-39} C m^2, -1.74×10^{-39} C m^2, and zero, respectively. It is important to note that many other parameter sets also give comparable least-squares errors but these ten are chosen based on their diverse optimized parameter sets.

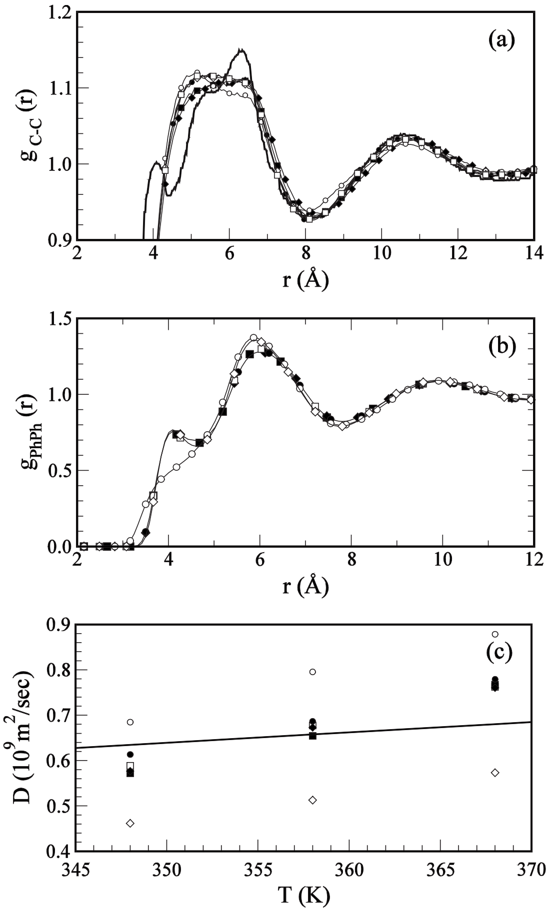

FIG. 3. Validating the ring models. (a) Comparison between the C-C radial distribution function of liquid benzene (bold line) at 300 K from x-ray data [54] and those from simulations. (b) Phenyl ring center-ring center radial distribution function for liquid biphenyl at 348 K and 0.9914 g/mL. (c) Self-diffusion coefficient of liquid biphenyl from MD simulations and experiment [66] (solid line). Results for six ring models are shown: A (filled squares), A2 (filled diamonds), B1 (open squares), B2 (filled circles), B3 (open diamonds), and C (open circles).

A comparison between carbon-carbon radial distribution functions $g_{CC}(r)$ is shown in Fig. 3(a). The experimental distribution function shows a peak at 4 Å, a shoulder at 5.5 Å, and a prominent peak at 6.2 Å. These "close contact" features are most sensitive to the atomic structure of the ring. As a result, the ellipsoidal ring model cannot fully capture these structural details and predicts instead a broad peak between 5.4 and 6.3 Å. Beyond this region, the GB model does well and reproduces the intermolecular details of the solvation shells. It is interesting to note that ring models that do not include a quadrupole moment are consistently inferior with predictions of an understructured fluid.

For the ten models, the self-diffusion coefficient of liquid benzene has been calculated from the slope of the mean-square displacement. Experimental values [60–63] range from 2.13×10^{-9} to 2.27×10^{-9} m^2/s. Simulations [55–58] typically underestimate self-diffusion in benzene. For instance, Kim *et al.* [58] performed a simulation of bulk benzene using a flexible atomistic model and predicted 1.25×10^{-9} m^2/s. The ten ring models under consideration predict diffusion coefficients between 0.60×10^{-9} and 1.29×10^{-9} m^2/s. Based on this, the four models with the smallest self-diffusion coefficients have been eliminated from further consideration. To summarize, our studies of benzene began with 6561 different models and finished with six.

Simulations of liquid biphenyl were performed to further refine the ring model. We have adopted the inter-ring torsional parameters [Eq. (2)] from Cacelli and Prampolini [64] and the ring centers are 4.279 Å apart [65]. The six selected parameter sets have been used in *NVT* MD simulations of 500 biphenyl molecules. The center-to-center radial distributions are given in Fig. 3(b). The models predict similar distributions except at small separations, where the shoulder at 4.2 Å is absent when the ring model does not include a quadrupole (C model). Closer inspection of snapshots indicates that this shoulder originates from crossed pairs of molecules and, as discussed below, this arrangement is energetically favored by the quadrupole.

The calculated self-diffusion coefficients of liquid biphenyl at 348, 358, and 368 K are compared to experiment [66] in Fig. 3(c). It is interesting and encouraging to note that the agreement with experiment is significantly better for biphenyl than for benzene. Four of the six parameter sets have been retained based on this comparison. These are termed A, B1, B2, and C and will be examined in details in Secs. III and IV. Models A and B2 differ only in the value of the ring quadrupole: the quadrupole on B2 is 20% smaller. Likewise, models B1 and C share the same GB parameters but only B1 is quadrupolar. Models B1 and B2 have identical quadrupole moments but differ in their GB parameters. The relationships between these models allow for an analysis of the impact of the quadrupole moment and the GB parameter sets. The four sets of ring parameters are listed in Table I.

TABLE I. Four selected sets of parameters for the ring models. Parameters are defined in the Appendix.

Parameter	A	B1	B2	C
ε_0 (kJ/mol)	3.1606	3.1606	3.1606	3.1606
σ_0 (nm)	0.6674	0.6674	0.6674	0.6674
$\varepsilon_0^{ss}/\varepsilon_0^{ee}$	3.5088	3.5088	3.5088	3.5088
$\sigma_0^{ee}/\sigma_0^{ss}$	0.4465	0.4465	0.4465	0.4465
ξ	0.5671	0.5671	0.5671	0.5671
μ	−2.5102	−2.0081	−2.5102	−2.0081
ν	0.2456	0.3070	0.2456	0.3070
Q (10^{-39} C m^2)	−2.1930	−1.7544	−1.7544	0.0000

D. Semi-coarse-grained 2PhP and 5PhP models

The final semi-coarse-grained interaction potentials for 2PhP and 5PhP contain intramolecular terms, controlling the energetic costs for molecular conformations, and intermolecular terms, accounting for the interactions between all pairs of atoms on different molecules or within the same molecule if the atoms are not very close to each other. In this regard, atoms or rings separated by fewer than four bonds are "close." The full potential is given by

$$U=\sum_{i=1}^{N_{ch}}\sum_{j>i}^{N_{ch}}U_{ij}^{Coul}+\sum_{i=1}^{N_{\mathrm{LJ}}}\sum_{j>i}^{N_{\mathrm{LJ}}}U_{ij}^{\mathrm{LJ/LJ}}+\sum_{i=1}^{N_{\mathrm{LJ}}}\sum_{j=i}^{N_{\mathrm{GB}}}U_{ij}^{\mathrm{LJ/GB}}+\sum_{i=1}^{N_{\mathrm{GB}}}\sum_{j>i}^{N_{\mathrm{GB}}}U_{ij}^{\mathrm{GB/GB}}+\sum_{i=1}^{N_{bends}}U_{bending}+\sum_{i=1}^{N_{dihedrals}}U_{torsion}, \tag{8}$$

where N_{ch}, N_{LJ}, N_{GB}, N_{bends}, and $N_{dihedrals}$ are the number of charges, Lennard-Jones (LJ) sites, GB sites, bends, and dihedral angles, respectively. The first sum runs over pairs of charge-bearing sites. For the rings, a partial charge equal to the sum of the net charges on the ring atoms is placed at the center of the ring. This charge differs for phenyl and pyrimidine. Alkyl-alkyl interactions are captured by the second sum which is a LJ potential that applies to interactions between pairs of chain atoms. Likewise, the third sum includes chain-ring interactions and nonelectrostatic ring-ring interactions are captured by the fourth sum. The energetic cost associated with bends and torsions within the mesogens is contained in the final two terms.

Returning to the ring representation, the inclusion of a ring quadrupole means that multipolar interactions include charge-charge, charge-quadrupole, and quadrupole-quadrupole terms. Only the last of these was present for the model tests on benzene and biphenyl. For 2PhP and 5PhP, we have chosen to replace each point quadrupole by four charges placed above and below the ring plane, along the symmetry axis $\hat{u}_A$. The charges are defined so that they exactly reproduce the desired quadrupole moment, have a net charge of zero, do not introduce a net dipole on the ring, and they are located close to the ring center inside the repulsive wall of the GB potential. Specifically, the charges are located at ±1 and ±0.5 Å on the ring axis and the magnitudes of the charges are ±0.9101 $|e|$ for model A and ±0.7281 $|e|$ for models B1 and B2. This simple representation of the ring quadrupole allows the use of charge-charge Ewald summations for all electrostatic interactions within the fluid. Thus, all multipolar interactions are included via the first sum in Eq. (8).

The phenyl and pyrimidine ring models are very similar but not identical. Specifically, they differ in the magnitude of the ring charge and in their associated intramolecular potentials. The current models do employ identical ring quadrupoles and GB potential parameters and, likely, the differences between the rings are underestimated.

III. SIMULATION DETAILS

A. Order and structure in the liquid-crystal phases

The properties employed to assess fluid structure, quantify order, and differentiate between phases are discussed in this section. Our evaluation of molecular organization begins with order parameters. Specifically, a molecular orientation vector, or local director, is defined and the correlation between these vectors is evaluated. For the current study, the most relevant vector joins the phenyl and the pyrimidine rings in the molecular core. With this chosen molecular vector, $\vec{u}_\alpha(t)$, the instantaneous average of all these vectors in the simulation cell defines a director, $\vec{D}(t)$. Order with respect to this director is assessed by evaluating

$$P_n^D(t) = \frac{1}{N}\sum_{\alpha=1}^{N} P_n(\cos\,\theta_\alpha), \tag{9}$$

where the sum runs over all N molecules, $P_n(\cos\,\theta)$ is a Legendre polynomial, and $\cos\,\theta_\alpha = [\vec{u}_\alpha(t)\cdot\vec{D}(t)]/(uD)$. The order parameter is largest when the molecular vectors are perfectly aligned with the director. We evaluate $P_n^D(t)$ for $n=1-4$ and report the instantaneous and time-averaged order parameters, $P_n^D(t)$ and $P_n^D = \langle P_n^D(t)\rangle$, respectively, in Sec. IV.

Following others [67], the director is obtained by evaluating the Q tensor

$$Q_{\alpha\beta}(t) = \frac{1}{2N}\sum_{\alpha=1}^{N}[3u_{\alpha a}u_{\alpha b} - \delta_{ab}], \quad a,b = x,y,z, \tag{10}$$

where the sum runs over all N molecules in the system and $u_{\alpha a}$ is the a component of $\vec{u}_\alpha(t)$. The largest eigenvalue of the Q tensor corresponds to $P_2^D(t)$ and the corresponding eigenvector is the director, $\vec{D}(t)$.

The presence of a nonzero order parameter reflects long-ranged correlations in molecular orientations. For a Sm-A phase, the molecular orientation is, on average, perpendicular to the layer plane so that the layer normal and the director coincide. This is not the case for a Sm-C phase. The instantaneous layer normal, $\vec{L}(t)$, was calculated within the simulations to identify the presence of Sm-C layers. The layer normal is conceptually intuitive but difficult to calculate within a simulation of complicated mesogens. After several attempts, we chose to define local layers normal, $\vec{l}_i(t)$, for each molecule and evaluate the overall layer normal, and associated $P_2^L(t)$ order parameter by replacing $\vec{u}_\alpha(t)$ with $\vec{l}_i(t)$ in Eq. (10). Specifically, the local layer normal calculation about a given molecule proceeds as follows: a site within the molecular core is chosen, the position of this site along with the positions of all equivalent sites within nearby molecules are least-squares fitted to a plane, and the vector normal to this plane is defined as the local layer normal. We found that choosing either the phenyl or pyrimidine ring center yielded equivalent results, as did the normal defined using the midpoint of the ring centers. All results reported in Sec. IV correspond to layers normal defined by the positions of the phenyl ring centers with neighboring centers included if their phenyl ring is within 6.36 Å of the central phenyl ring. This distance is chosen such that at least two molecules are generally found within the volume but molecules from neighboring smectic layers are too far away to contribute to the calculation of the local layer normal. In cases where too few neighbors are found, the molecule is not assigned a local layer normal. The present approach to defining a layer normal has the advantage of also yielding an associated order parameter. In this way, we can assess the consistency between local layers normal within the simulation cell.

Structural information is obtained by evaluation of pair functions. The simplest of these is the radial distribution function, $g(r)$, which gives the probability of finding a particle at a distance r from another, irrespective of their relative orientations [67]. The second-order correlation function, $g_2(r)$, is also evaluated

$$g_2(r) = \langle P_2(\cos\,\theta_{\alpha\beta})\rangle_r, \tag{11}$$

where $\theta_{\alpha\beta}$ is the angle between the core vectors, $\vec{u}_\alpha(t)$, of molecules α and β. $g_2(r)$ describes the average relative orientation of molecules separated by a distance r. This function vanishes when the molecular orientations are uncorrelated, reaches -0.5 when the molecules are in an orthogonal arrangement, and is unity when all molecules are perfectly aligned. $g_2(r)$ is short ranged in the isotropic phase but the range increases for nematic and smectic phases, approaching the square of P_2^D at large separations [67]. In this work, we report angular correlations between the molecular cores, as specified by the phenyl(6)-pyrimidine(7) axis.

The anisotropy of liquid-crystal phases requires the introduction of additional distribution functions to differentiate between phases. In Sec. IV, we report distributions resolved along the director, $\vec{D}(t)$, and along the layer normal, $\vec{L}(t)$. For each of these, all intermolecular distributions are subdivided into components parallel and perpendicular to the vector. Figures 4(a) and 4(b) illustrate the separation of an interparticle vector according to a layer normal and a director, respectively. We define a longitudinal radial distribution function, $g_\parallel^{D/L}(r_\parallel)$, as [68]

$$g_\parallel^{D/L}(r_\parallel) = \frac{\langle n\rangle_{r_\parallel,r_\parallel+\delta r_\parallel}}{\langle n_0\rangle_{r_\parallel,r_\parallel+\delta r_\parallel}}, \tag{12}$$

where $r_\parallel$ is the component of the interparticle separation resolved along the chosen vector, $\langle n\rangle_{r_\parallel,r_\parallel+\delta r_\parallel}$ is the number of intermolecular pairs with a projection along the vector between $r_\parallel$ and $r_\parallel+\delta r_\parallel$, and $\langle n_0\rangle_{r_\parallel,r_\parallel+\delta r_\parallel}$ is the corresponding number expected in an unstructured fluid. Analogously, a transversal radial distribution function, $g_\perp^{D/L}(r_\perp)$, is evaluated as

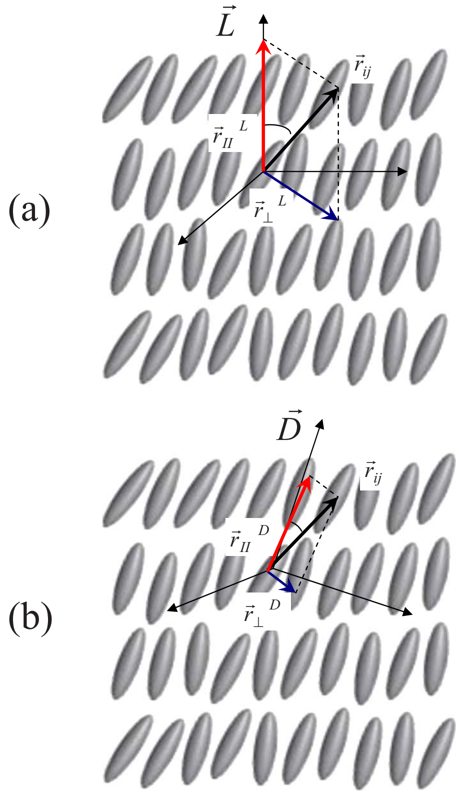

FIG. 4. (Color online) Schematics showing the decomposition of the interparticle vector, identified by a thick black arrow, according to (a) the layer normal and (b) the director.

$$g_{\perp}^{D/L}(r_{\perp}) = \frac{\langle n\rangle_{r_{\perp},r_{\perp}+\delta r_{\perp}}}{\langle n_0\rangle_{r_{\perp},r_{\perp}+\delta r_{\perp}}}, \tag{13}$$

where $r_{\perp}$ is the component of the interparticle separation resolved perpendicular to the vector, $\langle n\rangle_{r_{\perp},r_{\perp}+\delta r_{\perp}}$ is the number of intermolecular pairs with a projection perpendicular to the vector, and $\langle n_0\rangle_{r_{\perp},r_{\perp}+\delta r_{\perp}}$ is the corresponding value in an unstructured fluid.

The director and layer normal coincide in a Sm-*A* phase and either vector may be chosen to analyze the fluid structure. That is, $g_{\parallel}^{D}(r_{\parallel})$ and $g_{\parallel}^{L}(r_{\parallel})$ should be equal, within statistical error, and either one can be used to describe interlayer structure. Likewise, $g_{\perp}^{D}(r_{\perp})$ and $g_{\perp}^{L}(r_{\perp})$ both describe the molecular distributions within the layers. In a Sm-*C* phase, the layer normal and director no longer coincide and parallel and perpendicular distributions relative to these vectors are distinct.

The assessment of the angle between the director and the layer normal is central to differentiating between Sm-*C* and Sm-*A* phases. This is challenging within a simulation since entire layers may be tilted relative to each other due to constraints imposed by the size and shape of the simulation cell. Consider the following two definitions of the relative angle:

$$\Theta_1 = \langle \cos^{-1}(\vec{D}(t)\cdot\vec{L}(t))\rangle, \tag{14}$$

$$\Theta_2 = \frac{1}{N}\left\langle \sum_{\alpha=1}^{N} \cos^{-1}\{\vec{u}_{\alpha}(t)\cdot\vec{l}_{\alpha}(t)/(u_{\alpha}l_{\alpha})\}\right\rangle, \tag{15}$$

where the angular brackets denote time averaging. For Θ_1, all molecules first contribute to the global director and to the global layer normal. The relative angle is calculated based on these average directions. This method implicitly includes any tilting between layers and averages over local effects. The second method, yielding Θ_2, is based on local differences in molecular tilt and local layering. Equation (15) will yield angles that are insensitive to relative layer orientations.

When all local layers normal coincide with all local directors, Θ_1 and Θ_2 will both average to zero. If the local layers are always perpendicular to the molecular director, then Θ_2 will average to 90. These results are straightforward but, since the local layer normal can point in either direction (up or down from the layer), an ambiguity results in the calculation of Θ_2. By convention, we always choose the smallest angle between the local layer normal, $\vec{l}_{\alpha}(t)$, and the local director, $\vec{u}_{\alpha}(t)$, so that completely random relative orientations yield a value of 57.2957 for Θ_2.

A third approach to relative angle calculation is to employ distribution functions, specifically $g_{\parallel}^{D}(r_{\parallel})$ and $g_{\parallel}^{L}(r_{\parallel})$. The peak position in the former will appear at longer separations than for the latter in a smectic-*C* phase [see Figs. 4(a) and 4(b)]. The angle extracted from these peak positions is directly comparable to the tilt angle obtained from optical measurements.

Structure within the tail regions is assessed by collecting interatomic distributions between tail atoms. Order parameters are also collected for the alkoxy tails by applying Eqs. (9) and (10) for neighboring carbon atoms in the tails. Specifically, following the numbering in Fig. 1, we monitor the C(1)-C(2) and C(15)-C(16) vectors and report their order parameters.

B. MD simulations

Simulations of 2PhP and 5PhP are challenging due to many factors. These include slow dynamics for some motions within smectic phases, difficulty equilibrating from the initial configurations, and thermodynamic constraints on the phases formed due to the limited number of molecules in the simulation cell and the shape of the simulation cell. In this section, we address these concerns.

The MDMC [69] program has been employed for the MD simulations of 2PhP and 5PhP. 2PhP is examined at four temperatures (335, 365, 400, and 450 K) which spans the temperature range for Sm-*C*, Sm-*A*, nematic, and isotropic phases. The specific temperatures chosen do not coincide with the narrow nematic phase and we have not found a nematic within our simulations. 5PhP is examined at 370, 400, and 450 K where Sm-*A* and isotropic phases are observed experimentally [24]. Results are presented for simulations of 256 molecules. This number of molecules is sufficient for three to four layers to form within the simulation cell.

An isotropic starting configuration is ideal but we found that, even after introducing annealing steps into the equilibration process, equilibration was far too slow. Specifically, the disentanglement time required for these long molecules was too high. As an alternative, we start our simulations from a nematic phase. The initial configuration is prepared as follows. The selected number of molecules (in this case 256) is aligned and placed on a rectangular lattice (1:1:2 side lengths). The simulation cell is then expanded until all molecular overlaps are eliminated. Sequential recompression of the cell proceeds in conjunction with Monte Carlo and MD cycles. Molecules are then assigned random linear and angular velocities, consistent with the temperature, and the equilibration begins. The starting configuration typically has a P_2 order parameter between 0.5 and 0.8 and visual inspection shows nematiclike positional order.

The starting procedure noted above is ideal for 2PhP and 5PhP since the latter does not have a stable nematic phase while the nematic phase of 2PhP is only stable over a very narrow temperature range. At the lower temperatures, where smectic phases are expected, we find that layers form very quickly. An equilibration period of 0.5 ns is sufficient as the density in the cell and the order parameters have stabilized after this time. The molecules are initially aligned, as noted above, and once the layers form, most molecules maintain their orientation for the duration of the simulations. Thus, the P_3 order parameter tends to be nonzero. The impact of this initial aligned configuration will be discussed in Secs. III C and IV but here we note that a few runs starting from an antiparallel molecular alignment were also performed and will be considered in Sec. III C.

Molecular dynamics simulations in the *NPT* ensemble generally employ isotropic volume changes [70]. A smectic phase is not well suited to these isotropic changes due to the different impact on the intralayer and interlayer spacings. An attempt to enlarge the cell, for example, may be favorable for the layer spacing but the additional space within the layers may be energetically unfavorable. Anisotropic changes, where only one cell dimension is changed, are far more appropriate since they allow independent adjustment of the interlayer spacing. The extended Lagrangian formalism can accommodate anisotropic changes in the simulation cell but the simulation becomes significantly more complicated [71,72]. We have opted instead to employ Monte Carlo volume changes. Specifically, at each iteration, a random number is generated to decide upon whether a volume change will be attempted. On average, an attempt is made every 256 iterations. If the volume will be changed, the cell dimension to be changed is decided randomly and the magnitude of the change is randomly chosen, subject to a maximum. The latter is adjusted during the equilibration so that the success rate is between 30% and 70%. The acceptance criterion for volume changes is [67]

$$\exp\left\{-\frac{U^{old}}{kT}+\frac{U^{new}}{kT}-\frac{p(V^{old}-V^{new})}{kT}+(n+1)\ln\left(\frac{V^{old}}{V^{new}}\right)\right\}, \tag{16}$$

where N is the number of molecules and the superscripts "old" and "new" refer to the original and the changed simulation cells, respectively.

Nosé-Hoover thermostats [73–77] are implemented to maintain the temperature of the fluid. In particular, separate rotational and translational thermostats have been implemented. For isotropic fluids, the use of independent thermostats should have little impact but, for the present study, separate thermostatting of translations and rotations ensures that the rings are not rotationally cold.

As discussed above, changes in the shape and size of the simulation cell are allowed within the simulation and these change the density of the fluids. Our starting density is 0.90 g/mL, which is close but slightly lower than densities employed for related mesogens [78]. For all simulations, the density rapidly drops to around 0.77 g/mL as the nematic starting configuration reorganizes into layers. The density then gradually increases back to between 0.88 and 0.92 g/mL, with the lower average density for model C at higher temperatures and the higher density for the quadrupolar models at 335 K.

Two types of simulations are performed: a series of short 2 ns runs and longer 20 ns runs. For the shorter runs, five independent runs are performed for 2PhP at 335 K, 2PhP at 365 K, and 5PhP at 370 K. Three independent simulations are performed at 400 K and results are presented from two independent simulations at 450 K. Averaged results from the independent simulations, for a given temperature and mesogen, are reported below. All 50 simulations are performed for the B1 and C ring models. The A and B2 ring models are studied only at 335 and 365 K for 2PhP and 370 K for 5PhP. In total, results from 80 2-ns simulations are reported below. These results are complemented by 20 ns runs for the B1 and C models of 2PhP at 365 K and 5PhP at 370 K.

A time step of 0.25 fs is chosen for the simulations. Interatomic distributions, inter-ring distributions, and the order parameters are evaluated every 100 iterations. Snapshots of the simulation cell are collected every 250 000 iterations.

C. Convergence issues

Figure 5(a) compares phenyl-phenyl radial distributions for five independent 2 ns simulations of 2PhP, at 365 K, as predicted from the B1 model. These distributions, and all ring-ring distributions shown below, report probabilities as a function of the distance between the ring centers. Clearly, the five simulations predict similar ring-ring distributions beyond separations of 6 Å. At closer distances, where the rings are in contact, the simulations show the same peaks but with some differences evident in their intensities. The average distribution from these five 2 ns simulations is compared to the distribution from a single 20 ns run in Fig. 5(b). The overall agreement between the two distributions is good with relatively small intensity differences observed. We conclude that multiple short simulations are a viable alternative to single long simulations for these smectic liquid crystals. The initial configurations for the simulations in Sec. IV have parallel molecules in the simulation cell. In principle, the starting configuration should have no impact on the fluid structure but layer reorganization is slow in these fluids and some dependence may remain. With this in mind, the impact of the starting configuration is explored in Fig. 5(c), where the

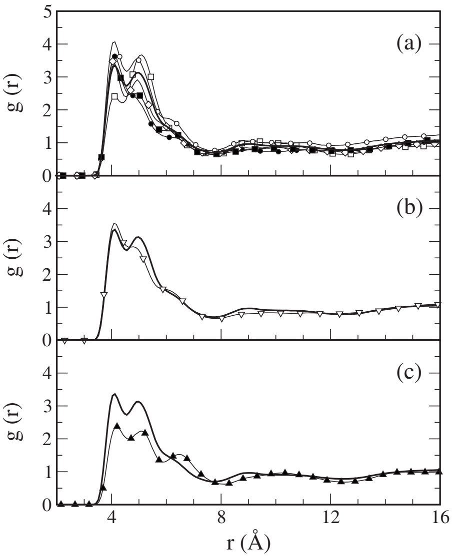

FIG. 5. Convergence tests, illustrated for 2PhP (B1 ring model) at 365 K. (a) Phenyl-phenyl radial distributions are shown for five independent 2 ns simulations (open circles, filled circles, open diamonds, open squares, and filled squares). Their average is shown with a thick solid line with solid circles. (b) Distribution from a single 20 ns simulation (open triangle down) is compared to the average distribution from independent 2 ns simulations (thick solid line). (c) Distribution functions for parallel (thick solid line) and antiparallel (filled triangle up) starting configurations.

phenyl-phenyl distribution is shown for a parallel and an antiparallel starting configuration. As will be discussed in Sec. IV A, the peak at roughly 6.5 Å is predominantly due to antiparallel neighboring molecules while parallel alignment contributes to the peak at 5 Å. Thus, the intensity differences in Fig. 5(c) are not unexpected. Overall, the differences observed in Fig. 5(c) are comparable to those in Fig. 5(a) and indicate that a parallel starting configuration is adequate.

The use of multiple short simulations provides a simple and efficient means of exploring the fluid structure. This is particularly true for 2PhP and 5PhP where equilibration from the nematic starting configuration is rapid. We employ five independent simulations for the lower temperatures, where smectic phases are expected, and two to three simulations at higher temperatures where isotropic phases occur. This number of simulations is sufficient to tentatively identify the phases and qualitatively analyze the fluid structure and order, but a greater number of simulations would be required to fully converge the properties of the fluid.

IV. RESULTS AND DISCUSSION

In this section, fluid structure and properties are analyzed in detail. The order in the core and tail regions, the dynamics of layer reorganization, the differences between 2PhP and 5PhP, and the impact of ring quadrupoles on fluid structure are discussed. Prior to examining the bulk fluids, we consider the energetics of relative arrangements within isolated molecular pairs. Following this analysis, for the sake of brevity, we will focus on the B1 model with comparisons to other models included as appropriate.

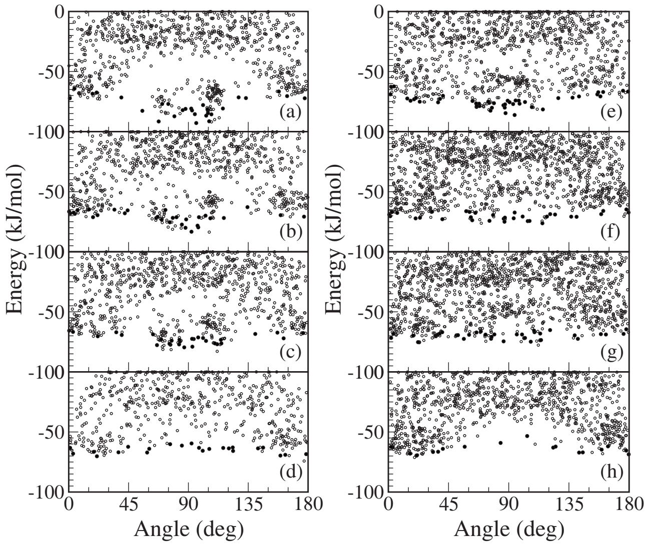

2PhP **5PhP**

FIG. 6. Pair energy plotted as a function of relative angle between two 2PhP molecules, obtained using the (a) A, (b) B1, (c) B2, and (d) C ring models, respectively. The pair energy plotted as a function of relative angle between two 5PhP molecules obtained using the (e) A, (f) B1, (g) B2, and (h) C ring models, respectively. Each open dot represents an energy minimization following a random initial structure of the dimer. Each filled circle represents the lowest energy achieved for a fixed relative angle.

A. Pair energies

It is instructive to begin by considering interactions between pairs of 2PhP and 5PhP molecules. We have undertaken "docking" studies to identify the most energetically favored molecular arrangements. Specifically, two molecules are positioned randomly at the center of a very large simulation cell and MD simulations are performed as the temperature is gradually decreased to around 2 K. These simulations are repeated between 800 and 1850 times using new random starting arrangements. The final energies, as a function of the core-core angle, are represented by open circles in Fig. 6. In addition, a few values for the intercore angles were selected and, for these angles, several hundred simulations were performed. The lowest energies achieved from these simulations are represented by filled circles in the figure.

Figure 6(a) shows the results of docking studies for 2PhP when the A ring model is used. Of the four ring models, this one has the largest value of the ring quadrupole. The figure shows that crossed molecular cores have the lowest pair energy. The density of points in this region, along with its separation from the rest of the points, indicates that this conformation may be somewhat difficult to reach, relative to conformations where the cores are roughly parallel. When the ring quadrupole decreases, the energetic bias toward crossed arrangements also decreases and this is evident by the smaller energy gap for parallel versus crossed arrange-

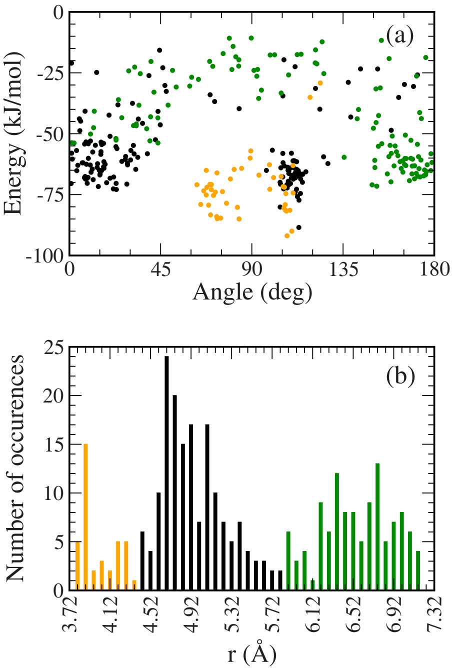

FIG. 7. (Color online) Pair energy plotted (a) as a function of relative angle between two 2PhP molecular cores and (b) as a function of phenyl-phenyl ring separation. Results are presented for the A model. Each dot in (a) represents an energy minimization following a random initial structure of the dimer. In (a), yellow (light gray), black, and green (dark gray) circles identify configurations where the phenyl-phenyl distance is between 3.4–4.4 Å, 4.4–5.8 Å, and 5.8–7.2 Å, respectively. Only configurations with a pair energy less than −10 kJ/mol contribute in (b).

ments when the B1 and B2 ring models are used [see Figs. 6(b) and 6(c)]. This bias vanishes entirely in the absence of a ring quadrupole (C ring model).

Figure 6(a) is reproduced in Fig. 7(a) with color coding introduced to separate the points according to the distance between the phenyl rings. Green identifies that the rings are within 3.4 and 4.4 Å, and this occurs exclusively for crossed configurations with a relative core angle around 70° with the phenyl rings closer together. At slightly larger distances, between 4.4 and 5.8 Å, two configurations contribute. Either the molecules are roughly parallel, with face-to-face phenyl rings, or a crossed configuration with intercore angle of around 110° occurs (“anticrossed”). At larger distances, between 5.8 and 7.2 Å, antiparallel configurations appear along with less energetically favorable parallel and crossed configurations. The latter tends to have an intercore twist so that edge-to-face ring arrangements occur.

Figure 7(b) recategorizes all the minima according to the distance between the phenyl rings. Three well-defined peaks are evident around 4, 5, and 6.4 Å. We conclude that only crossed-core configurations occur at small separations, parallel and anticrossed configurations occur between 4.4 and 5.8 Å, and antiparallel configurations are the largest contributor between 5.8 and 7.2 Å. The correlation between phenyl-phenyl ring distance, pair energy, and intercore angle in Fig. 7 will prove useful in understanding the fluid structure in the liquid crystalline phases of 2PhP and 5PhP discussed in the following sections.

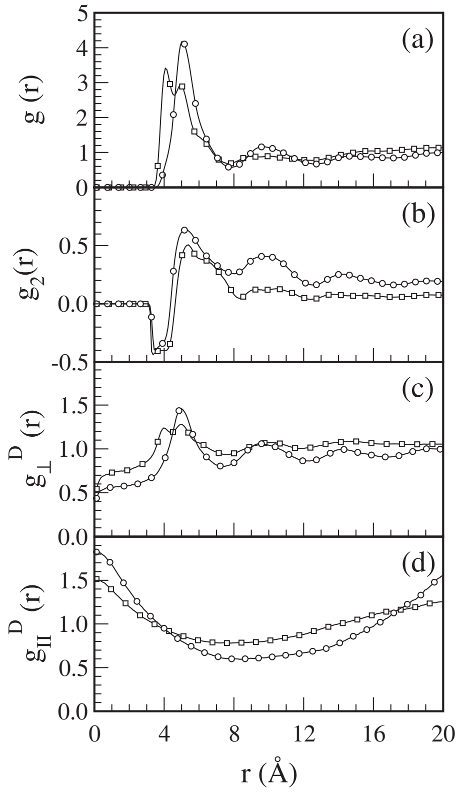

FIG. 8. Impact of the ring quadrupole on the liquid-crystal phase of 2PhP at 365 K. Phenyl-phenyl distributions are compared for models B1 (open squares) and C (open circles). Radial distributions, orientational distributions, structure perpendicular to the director, and structure parallel to the director are compared in (a), (b), (c), and (d) respectively.

Comparing between 2PhP and 5PhP, the quadrupole has a larger energy-lowering effect for 2PhP. This is an important difference between the mesogens: 2PhP molecules will have a tendency to adopt crossed-core arrangements in the fluid. In contrast, neighboring 5PhP molecules are expected to have a more even distribution of core angles. The latter occurs as a result of the nonplanarity of the core region in 5PhP which frustrates, to a significant extent, the energy lowering that can be achieved by crossed-core arrangements. Overall, entropy favors parallel and antiparallel molecular arrangements but, particularly for 2PhP, energetics favor crossed-core arrangements.

B. Impact of ring quadrupoles

Figure 8 illustrates the impact of the ring quadrupole by examining the phenyl-phenyl distribution of 2PhP at 365 K. Specifically, the figure compares radial distributions $g(r)$, the orientational distribution $g_2(r)$, the distribution along the director $g_{\parallel}^{D}(r_{\parallel})$, and the distribution perpendicular to the director $g_{\perp}^{D}(r_{\perp})$ for the B1 and C ring models, which differ only by the absence of a quadrupole for the latter.

The addition of a quadrupole to the ring has a dramatic impact on the fluid structure. Without a quadrupole, the phenyl-phenyl radial distribution has a simpler structure with a side-by-side contact peak at 5 Å and a second peak at

9.5 Å. The contact peak corresponds primarily to parallel molecular cores, with the possibility of some contribution from anticrossed pairs. The presence of a quadrupole on the ring splits the contact peak, with the introduction of a feature at 4 Å. This peak is due to crossed molecular pairs that, according to Fig. 6(b), are now energetically favored. A slight shoulder at 6.2 Å also appears. The first minimum in the radial distribution appears at 7.8 Å regardless of the ring model. We can therefore easily and directly compare coordination numbers, obtained from integrating $g(r)$ between 0 and 7.8 Å. We find that, on average, a given 2PhP molecule has 4.4 nearest neighbors regardless of the presence of the quadrupole. Thus, the quadrupole dramatically alters the relative orientation of the nearest neighbors without changing the overall number of neighbors.

Second-order correlations are shown in Fig. 8(b). At large distances, $g_2(r)$ approaches $(P_2^D)^2$. This limit is clearly higher in the absence of the ring quadrupole indicating a more ordered fluid. Structure perpendicular and parallel to the director [see Figs. 8(c) and 8(d)] is also stronger in the absence of the quadrupole. All of these features are indicative of a simpler layer structure, with more order within the layers, when the rings do not include quadrupoles. It is important to realize, however, that the director is defined by the molecular core and, with the introduction of crossed configurations, the fluid structure is more complex rendering the assessment of core order more problematic.

An analysis of the 2PhP and 5PhP phases predicted from the C ring model shows that only Sm-*A* phases are predicted at all temperatures, even 450 K where an isotropic fluid is expected (see Fig. 1). This model clearly predicts too much order in the fluid and does not provide a satisfactory representation of the 2PhP and 5PhP mesogens. We conclude that the quadrupolar nature of the rings is an essential contributor to the phases of 2PhP and 5PhP.

C. Structure and order

Figure 9 compares distributions within the core region to distributions in the tails. Specifically, distributions between C(1)-C(1) and C(16)-C(16), the end groups in the hydrocarbon tails, are compared to the core phenyl-phenyl and pyrimidine-pyrimidine distributions. From the radial distributions in Fig. 9(a), the C(1)-C(1) and C(16)-C(16) distributions are similar even though the tails differ in length (see Fig. 1). In both cases, the radial distributions are liquidlike with a broad contact peak at around 4.3 Å and a weak secondary peak at around 8.5 Å. Unlike typical liquid distributions, the radial distribution function shows a broad region of low probability between 10 and 20 Å corresponding to separations where the aromatic molecular cores are found. The ring-ring distributions are, by contrast, more structured with pronounced contact and secondary peaks. As with the end groups, the distributions show a broad region of low probability. In this case, the region corresponds to separations where alkoxy tails are found in the layered fluid.

The distribution functions can be subdivided into components parallel and perpendicular to the director. The component perpendicular to the director, given in Fig. 9(b), shows that the 5PhP rings have a well-defined intralayer structure with three peaks evident at 5, 10, and 15 Å. These peaks correspond to neighbor, next-nearest neighbor, and next-next-nearest neighboring rings in the layer. In contrast, the distributions between tail atoms indicate that their structure is short ranged and weaker: $g_{\perp}^D(r_{\perp})$ shows very little structure beyond a small contact peak due to neighboring molecular tails. Structure along the director, shown in Fig. 9(c), reflects the interlayer spacing and has, as expected, a similar distribution for both core and tail regions.

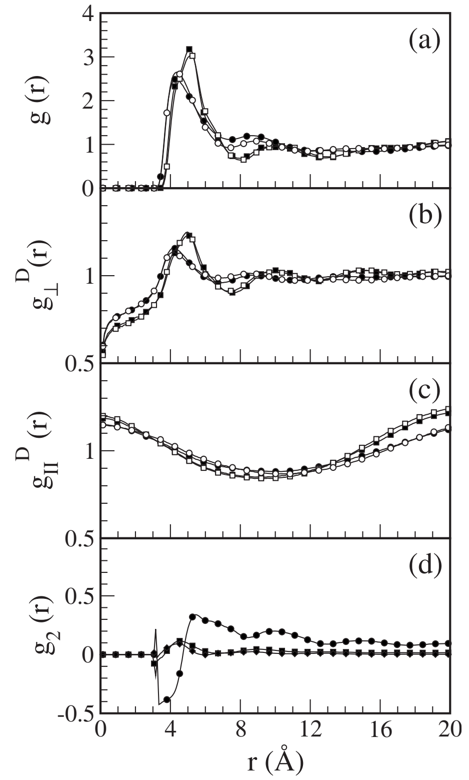

FIG. 9. Comparison between tail and core structures in the 5PhP liquid-crystal phase at 370 K as predicted from the B1 model. In (a), (b), and (c), distributions between C(1)-C(1), phenyl-phenyl, pyrimidine-pyrimidine, and C(16)-C(16) are shown by solid circles, solid squares, open squares, and open circles, respectively. Panel (a) compares radial distribution functions while perpendicular and longitudinal distributions, relative to the director obtained from phenyl-pyrimidine core axes, are shown in (b) and (c). Panel (d) shows intermolecular orientational distribution functions as determined from the phenyl-pyrimidine axis (solid circles), C(1)-C(2) axis (solid squares), and the C(15)-C(16) axis (solid diamonds).

Although the phenyl-pyrimidine axis is the most obvious choice for defining a director, other choices can be made. Directions defined from the C(1)-C(2) and C(15)-C(16) bonds have been chosen for comparison. Figure 9(d) shows the angular correlation between these chosen axes within neighboring molecules. The intercore axis distribution shows that, when the molecular cores are very close together, they adopt a crossed configuration. If all molecules adopted this configuration, then $g_2(r) \rightarrow P_2(\cos\,\theta) \rightarrow -0.5$. From the figure, the angular correlation between phenyl-pyrimidine axes approaches this limit at small separations. The intercore $g_2(r)$ quickly becomes positive at larger separations as parallel

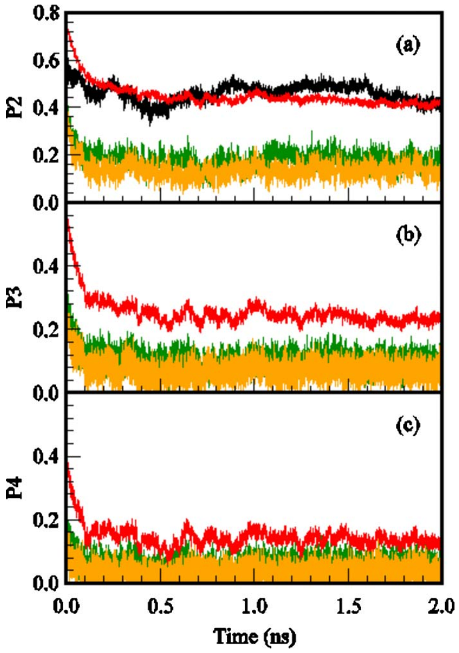

FIG. 10. (Color online) Time evolution of order parameters for 5PhP, at 370 K, as represented by the B1 model. Order relative to the vectors defined from the phenyl-pyrimidine, C(1)-C(2), and C(15)-C(16) axes are represented in red (upper line, gray), green (lower line, gray), and yellow (light gray), respectively. The P_2, P_3, and P_4 order parameters are shown in (a), (b), and (c), respectively. In (a), the P_2 order parameter describing the consistency between local (molecular) layers normal is shown in black.

core arrangements begin to contribute to the orientational distribution. In contrast, the alkoxy tails show very little orientational correlation except at very small separations. The orientational distribution function tends to $\langle P_2\rangle^2$ at large separations and Fig. 9(d) shows that the molecular cores have long-ranged orientational order but the tails do not.

The time evolution of the fluid order is shown in Fig. 10 for 5PhP at 370 K. The starting configuration for the simulation is a nematic fluid. For the simulation shown, the starting $P_2^D(t)$ order parameter is 0.75 for the core axis and quickly drops to between 0.4 and 0.5. This pattern is consistent for all our simulations: the initial order is reduced once the molecules form the layered structure. In particular, the introduction of crossed configurations will lead to a reduction in $P_2^D(t)$ due to our protocol for evaluating the order rather than to a true reduction in order. The complexity of the molecular structure also leads to a lower order parameter and values observed for simpler models [32,79] are not expected to be observed here.

A $P_2^L(t)$ order parameter is also provided in Fig. 10. This quantity reflects consistency between the local layers normal, determined for each molecule by evaluating the normal to the plane defined by neighbor positions. For the simulation shown in Fig. 10(a), the consistency between the local layers normal is similar to the agreement between the inter-ring axes throughout the simulation. This is atypical and usually the layer normal has a significantly larger order parameter than the director with the discrepancy between $P_2^D(t)$ and $P_2^L(t)$ mostly due to the larger impact of crossed-core configurations on the former.

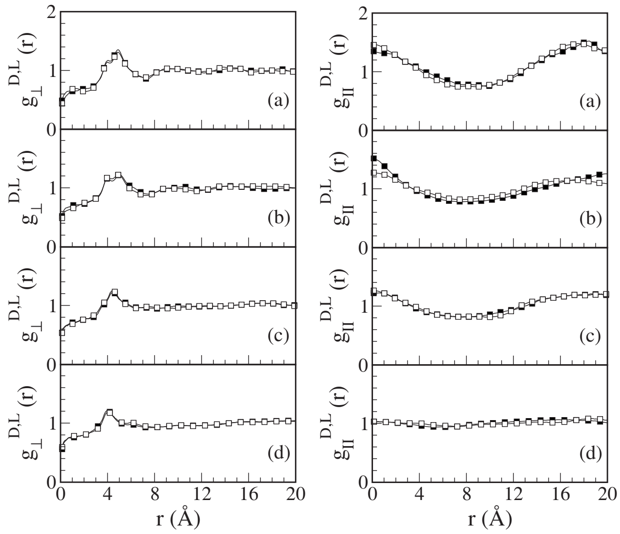

FIG. 11. Distribution between phenyl rings in 2PhP (B1 ring model) analyzed according to contributions perpendicular and parallel to the director and the layer normal. Results are shown for (a) 335 K, (b) 365 K, (c) 400 K, and (d) 450 K.

The P_2 order parameter obtained from the molecular tails is also shown in Fig. 10. It is consistently low (<0.2), as expected since the tails are less organized than the cores. However, P_2 is slightly larger for C(1)-C(2), the shorter tail, than for C(15)-C(16). It follows that the order in the tail region will be smaller for atoms or bonds that are farther from the molecular core: the core ordering is transferred, to some extent, to nearby bonds in the hydrocarbon chains. In 5PhP, a small amount of order remains for atoms five bonds away from the core but not for atoms nine bonds away.

The P_3 and P_4 order parameters are also provided in Fig. 10. P_4 is consistently higher for the director and near zero for the hydrocarbon tails. The P_3 order parameters are not zero as one would expect for these fluids, although they are small. When simulations are started with parallel or antiparallel molecules, the original alignment is partially preserved over a 2 ns simulation. To be more precise, for a parallel starting configuration, the P_3 order parameter drops initially as the fluid transitions away from a nematic to a smectic. Once the layers are formed, the P_3 order parameter stabilizes, as shown in Fig. 10(b), and further decreases are very slow. Clearly, if the original configuration was isotropic, then the molecules would align with random orientations since energetics do not favor a particular alignment (Fig. 6). A few simulations were also started with antiparallel molecules and, as expected, the P_3 order parameter is zero (aside from instantaneous fluctuations) throughout the simulation.

Together, Figs. 9 and 10 show that the alkoxy tail regions are liquidlike while the aromatic cores are ordered. This is evident from the structural measures shown in Fig. 9 and the order parameters in Fig. 10.

D. Layering and phase behavior

Figures 11 and 12 show the phenyl-phenyl ring distribution in 2PhP and 5PhP, subdivided according to components

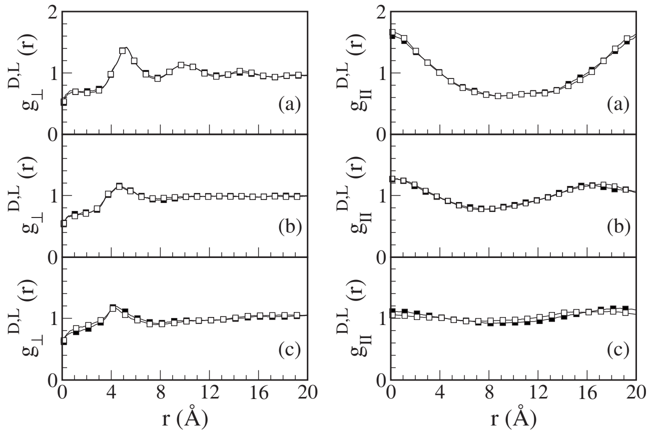

FIG. 12. Distribution between phenyl rings in 5PhP (B1 ring model) analyzed according to contributions perpendicular and parallel to the director and the layer normal. Results are shown for (a) 370 K, (b) 400 K, and (c) 450 K.

parallel and perpendicular to the layer normal and the director. Crossed intracore arrangements are most prominent for 2PhP at 335 and 365 K. This is evident from the peak at 4 Å in the intralayer distributions, $g_{\perp}^{D/L}(r_{\perp})$. As discussed in Sec. IV A, crossed configurations of 2PhP molecules originate from the combined effect of the ring quadrupoles and the inter-ring planarity that, together, leads to substantially lower pair energies for crossed-core pairs of 2PhP molecules. From Fig. 11, our simulations also suggest that the layer normal and the director are not equivalent for 2PhP at 335 and 365 K. This is evident from the small difference between $g_{\parallel}^{D}(r_{\parallel})$ and $g_{\parallel}^{L}(r_{\parallel})$. At 365 K, the latter indicates that the layers are roughly 16 Å apart whereas the former indicates a separation of 20 Å. From these peak positions, we calculate a relative tilt angle of roughly 37°. These distributions coincide at 400 K, as expected for a Sm-*A* phase, and a layer spacing of 20 Å is predicted. Both $g_{\parallel}^{D}(r_{\parallel})$ and $g_{\parallel}^{L}(r_{\parallel})$ are nearly unity at 450 K indicating that the phase is isotropic at this temperature.

Layer spacing has been measured [22] for 2PhP at several temperatures. The experimental spacing is higher, varying from 24 Å in the Sm-*C* phase to 26 Å at the transition to Sm-*A*. Our calculated values show the correct increase with temperature near the Sm-*C* to Sm-*A* transition, but they are smaller. This is due, in large part, to some retention of the initial parallel molecular orientation. Specifically, the tails are not of equal length—they are roughly 5 and 10 Å long. An antiparallel, or randomized, starting configuration is predicted to lead to layer spacing of 21–27 Å in much better agreement with experiment.

Figure 12 shows that, at all three temperatures, the layer normal and the director are equivalent for 5PhP. As well, the layer spacing is predicted to decrease from 20 Å at 370 K to 17 Å at 400 K. While experimental layer spacings are not available for comparison, the spacing should decrease slightly with temperature. At 450 K, $g_{\parallel}^{D}(r_{\parallel})$ and $g_{\parallel}^{L}(r_{\parallel})$ are nearly unity and 5PhP is correctly predicted to be isotropic.

Our phase assignation, particularly between Sm-*C* and Sm-*A*, is tentative at this point. A considerably larger number of simulations would be required to definitively distinguish between these phases. However, given the complexity of these fluids, the results of Figs. 11 and 12 are encouraging. Our simulations capture differences in the intralayer fluid structure of 2PhP and 5PhP, reproduce the correct temperature dependence of the layer spacing, and identify the central role of ring quadrupoles. The B2 ring model, which differs from the B1 model only in the GB parameters, shows similar results although the differences between the layer normal and director distributions are very small for 2PhP at 335 and 365 K.

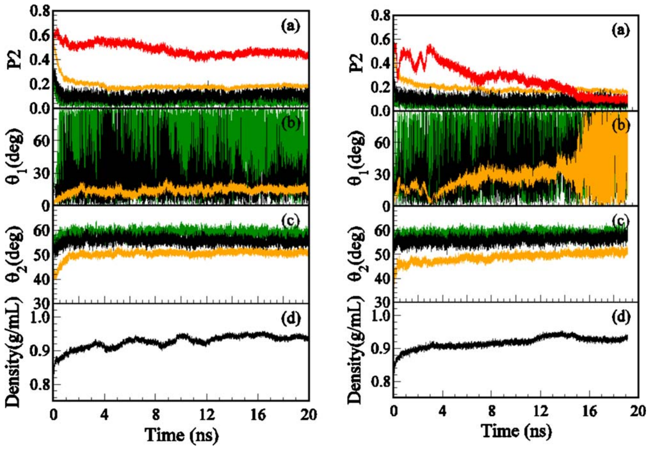

FIG. 13. (Color online) Instantaneous fluctuations for 2PhP at 365 K (left) and 5PhP at 370 K (right). Yellow (light gray), black, and green (dark gray) pertain to the phenyl-pyrimidine, C(1)-C(2), and C(15)-C(16) vectors in the molecule, respectively. Fluctuations in the order parameter associated with each of the vectors are shown in (a). Red line (upper line, gray) in the upper most panel shows fluctuations in the layer normal order parameter. The angles Θ_1 and Θ_2, evaluated from Eqs. (14) and (15), are given in (b) and (c). Instantaneous fluctuations in the density are shown in (d).

E. Dynamics

Longer 20 ns simulations were performed for 2PhP at 365 K and 5PhP at 370 K. These simulations provide some indication of the time scale for layer reorganization. Figure 13 shows the instantaneous variations in the density, the P_2 order parameter for the director and the layer normal, and the P_2 order parameter for the C(1)-C(2) and C(15)-C(16) bonds in the alkoxy tails. The variation in the Θ_1 and Θ_2 angles, calculated from Eqs. (14) and (15), are also shown.

The angle between the global layer normal and the global director is captured by Θ_1. All local contributions are averaged out for Θ_1, but contributions from imperfect layering will be observed. We calculate this angle for the director and also for the global vectors defined by the alkoxy tails, C(1)-C(2) and C(15)-C(16). The angle between the layer normal and the tail vectors oscillates rapidly between zero and 90°. This indicates that the ends of the alkoxy tails are mostly uncorrelated with the layering in the core region. The oscillations are somewhat larger for C(15)-C(16) since these atoms are further removed from the molecular core. The cor-

TABLE II. Average tilt angles, in degrees, P_2 order parameters for the director and the layer normal, the average density in g/mL, and the average potential energy in kJ/mol. The angles Θ_1 and Θ_2 are evaluated from Eqs. (14) and (15), respectively. The properties for 2PhP at 335 and 365 K and 5PhP at 370 K represent averages over five independent 2 ns simulations. Properties at 400 K are obtained from averages over three 2 ns simulations while 450 K properties are obtained from averages over two 2 ns simulations.

	2PhP results for each ring model				5PhP results for each ring model			
Property	A	B1	B2	C	A	B1	B2	C
	335 K							
Θ_1	11	7	7	8				
Θ_2	48	44	46	43				
P_2^D	0.21	0.33	0.27	0.44				
P_2^L	0.50	0.55	0.55	0.47				
$\langle\rho\rangle$	0.89	0.92	0.91	0.89				
$\langle U\rangle$	−138	−152	−146	−124				
	365 K				370 K			
Θ_1	12	9	12	7	14	14	15	10
Θ_2	49	46	46	42	46	45	46	43
P_2^D	0.17	0.26	0.23	0.43	0.23	0.31	0.26	0.51
P_2^L	0.45	0.52	0.50	0.49	0.39	0.42	0.41	0.48
$\langle\rho\rangle$	0.89	0.90	0.90	0.89	0.89	0.89	0.89	0.87
$\langle U\rangle$	−140	−133	−133	−117	−131	−126	−125	−115
	400 K				400 K			
Θ_1		8		4		11		17
Θ_2		49		43		48		46
P_2^D		0.19		0.45		0.20		0.31
P_2^L		0.51		0.53		0.45		0.33
$\langle\rho\rangle$		0.89		0.88		0.88		0.86
$\langle U\rangle$		−117		−108		−117		−111
	450 K				450 K			
Θ_1		23		8		32		10
Θ_2		52		49		52		44
P_2^D		0.12		0.36		0.12		0.51
P_2^L		0.34		0.34		0.30		0.49
$\langle\rho\rangle$		0.87		0.85		0.86		0.84
$\langle U\rangle$		−109		−92		−102		−102

relation between the director and the layer normal is, by contrast, evident in Fig. 13.

A local picture of molecular orientation is provided by the angle between the local layer normal and the local director. The average of these angles is captured by Θ_2 in Fig. 13. This angle is also calculated for the alkoxy tails, relative to the local layer normal, and the results show an average of 55°–60°. As discussed below Eq. (15), if the tail orientations are uncorrelated with the local layer normal, an average angle of 57.3° is expected. This is clearly the case for C(15)-C(16) and nearly true for C(1)-C(2) indicating, once again, that the alkoxy tail region is liquidlike. For the local director, defined by the phenyl-pyrimidine axis, a correlation with the local layer normal is evident from the deviation from 57.3°. Differences between 5PhP and 2PhP are present but relatively small.

The layers formed by 2PhP and 5PhP often do not conform to the simple layering patterns observed for single-site models [25,26]. Several factors contribute to the formation of partial and complex layers. First, the molecules are large and "perfect" layers may not be realistic for molecules of this complexity. Second, the dynamics of layer reorganization is slow. Nonetheless, the molecular cores clearly aggregate into layers with some crossed-core configurations and some parallel cores evident within the layers. Although the layers tend to align in parallel planes, this is not always the case, and partial layers may orient in several different directions. In this regard, the uppermost panel in Fig. 13 shows the P_2 order parameter for the layer normal, the director, and the C(1)-C(2) and C(15)-C(16) bonds in the alkoxy tails. The order is consistently near zero for the alkoxy tails and generally higher for the layer normal than for the director. The order parameters for 5PhP show stronger fluctuations and the order associated with the layer normal ultimately decreases to 0.1. At first glance, this would suggest complete dissolution of the layers and a transition to a nematic or an isotropic phase. A close inspection of snapshots reveals that the simulation cell consists of smaller, partial layers that are poorly aligned relative to each other. Thus, in this case, the order parameter does not reflect the presence of the layers but rather the consistency in their alignment. Once the fluid adopts this structure, at around 14 ns, the global layer normal begins to fluctuate rapidly causing Θ_1 to also fluctuate, since this quantity involves comparison to the global layer normal [see Eq. (14)]. The continued presence of regional layering is indicated by the time dependence of the local molecular structure (Θ_2 in panel C) showing that local environments are relatively stable over the 20 ns simulation.

Correlations between the panels in Fig. 13 are evident and transition regions, such as the dip in the 5PhP order parameter at 3 ns, provide a rough measure of the time frame for layer reorganization. This is only a rough guide however. Our 20 ns simulations reflect the challenges of simulating liquid crystals: some structural changes occur on the ns time scale but others require tens of nanoseconds. Single simulations would need to be exceedingly long to survey the thermodynamically accessible layered structures in the fluid. Our approach of using multiple short simulations is simple, but necessary, to glean details of the fluid structures of 2PhP and 5PhP.

Table II provides average angles, densities, potential energies, and order parameters with the quantities obtained by accumulating instantaneous values over multiple 2 ns simulations. As expected, the density and average potential energy decrease with temperature. The results from the C ring model indicate Sm-*A* phases at all temperatures since the orders associated with the layer normal and the director are, within statistics, indistinguishable and nonzero at all temperatures. For the A ring model, the five independent simulations are fairly distinct and the dynamics are slow. We suspect that the ring quadrupole is too large for this model. The properties evaluated from the B1 and B2 ring models are similar in most respects indicating that the GB parameters are less important, relative to the ring quadrupole, in determining fluid properties.

V. CONCLUSIONS

In this paper, the phases of 2PhP and 5PhP are examined in detail. Molecular dynamics simulations form the basis of the analysis, with Ewald summations for the electrostatics, anisotropic changes in the cell shape and size, and multiple thermostats for translation and rotation. The starting point is the design of an appropriate molecular model. A semi-coarse-grained model is adopted in the current study for practical reasons: quadrupoles are readily included for the aromatic rings and the models are more efficient than atomistic representations. 2PhP is explored at 335, 365, 400, and 450 K. Over this temperature range, this mesogen forms Sm-*C*, Sm-*A*, nematic, and isotropic phases. A closely related mesogen, 5PhP, is also examined at several temperatures. Specifically, we examine the fluid at 370, 400, and 450 K where Sm-*A* and isotropic phases are expected. A comparison of 5PhP and 2PhP is interesting since these two molecules are structurally very similar, with the most notable difference being a preference for planarity in the molecular core of 2PhP while 5PhP adopts a twisted-core conformation due to steric constraints.

Semi-coarse-grained models offer many advantages over atomistic and fully coarse-grained models. Specifically, they can be easily adapted to include ring quadrupoles while capturing molecular flexibility and remaining computationally feasible. The current models for 2PhP and 5PhP underestimate the differences between the phenyl and pyrimidine rings. Parametrization of a ring model for pyrimidine is an obvious route to improvement of the molecular model. In this work, model characterization via pair interactions proved to be essential in identifying and analyzing the short-range structure in the phases.

The essential results of this study can be summarized as follows. First, the presence of ring quadrupoles is essential to reproducing the phases of 2PhP and 5PhP. Without ring quadrupoles, only Sm-*A* phases occur and they persist to high temperatures where the true fluids are isotropic. Studies of pair energies indicate that the quadrupoles lead to energetically favored crossed-core configurations but that the energy lowering is much more significant for 2PhP. Simulations of the mesogens indicate that the tail regions are less structured, showing distributions consistent with isotropic fluids, and have no long-ranged order even when the cores are ordered. The simulations show that, at lower temperatures, the 2PhP and 5PhP phases are distinct with crossed-core configurations more probable for the former. Our simulations correctly capture expected trends in the layer spacing with temperature. Longer 20 ns simulations identify that layer reorganization is a slow process that requires up to tens of nanoseconds.

ACKNOWLEDGMENTS

Discussions with Professor Robert Lemieux are gratefully acknowledged. We also acknowledge the financial support of the Natural Sciences and Engineering Research Council (NSERC) of Canada and the generous allocation of computational resources at the Shared Hierarchical Academic Research Computing Network (SHARCNET), Westgrid, and the High Performance Computing Virtual Laboratory (HPCVL).

APPENDIX: THE GAY-BERNE POTENTIAL

The Gay-Berne potential is given in Eq. (3). Expressions for the parameters appearing in the distance dependent ratio [Eq. (4)] and anisotropic well depth [Eq. (5)] are provided in this appendix. In Eq. (4), the distance parameter $\sigma_{AB}(\hat{u}_A,\hat{u}_B,\hat{r}_{AB})$ is

$$\sigma_{AB}(\hat{u}_A,\hat{u}_B,\hat{r}_{AB}) = \sigma^0_{AB}\left[1-\left\{\frac{\chi_{AB}\alpha^2_{AB}(\hat{u}_A\cdot\hat{r}_{AB})^2+\chi_{AB}\alpha^{-2}_{AB}(\hat{u}_B\cdot\hat{r}_{AB})^2-2\chi^2_{AB}(\hat{u}_A\cdot\hat{r}_{AB})(\hat{u}_B\cdot\hat{r}_{AB})(\hat{u}_A\cdot\hat{u}_B)}{1-\chi^2_{AB}(\hat{u}_A\cdot\hat{u}_B)^2}\right\}\right]^{-1/2}, \tag{A1}$$

where $\chi_{AB}\alpha^2_{AB}$, $\chi_{AB}\alpha^{-2}_{AB}$, and χ^2_{AB} are calculated using combination rules suggested by Cleaver *et al.* [80]

$$\chi_{AB}\alpha^2_{AB} = \frac{(\sigma^{ee}_{AA})^2-(\sigma^{ss}_{AA})^2}{(\sigma^{ee}_{AA})^2+(\sigma^{ss}_{BB})^2}, \tag{A2}$$

$$\chi_{AB}\alpha^{-2}_{AB} = \frac{(\sigma^{ee}_{BB})^2-(\sigma^{ss}_{BB})^2}{(\sigma^{ee}_{BB})^2+(\sigma^{ss}_{AA})^2}, \tag{A3}$$

$$\chi^2_{AB} = \frac{[(\sigma^{ee}_{AA})^2-(\sigma^{ss}_{AA})^2][(\sigma^{ee}_{BB})^2-(\sigma^{ss}_{BB})^2]}{[(\sigma^{ee}_{AA})^2+(\sigma^{ss}_{BB})^2][(\sigma^{ee}_{BB})^2+(\sigma^{ss}_{AA})^2]}. \tag{A4}$$

The anisotropic well-depth parameter $\varepsilon_{AB}(\hat{u}_A,\hat{u}_B,\hat{r}_{AB})$ is a product of three terms. In Eq. (5), $\varepsilon^{(1)}_{AB}(\hat{u}_A,\hat{u}_B)$ is

$$\epsilon^{(1)}_{AB}(\hat{u}_A,\hat{u}_B) = [1-\chi^2_{AB}(\hat{u}_A\cdot\hat{u}_B)^2]^{-1/2} \tag{A5}$$

and

$$\varepsilon^{(2)}_{AB}(\hat{u}_A,\hat{u}_B,\hat{r}_{AB}) = 1-\left\{\frac{\chi'_{AB}\alpha'^2_{AB}(\hat{u}_A\cdot\hat{r}_{AB})^2+\chi'_{AB}\alpha'^{-2}_{AB}(\hat{u}_B\cdot\hat{r}_{AB})^2-2\chi'^2_{AB}(\hat{u}_A\cdot\hat{r}_{AB})(\hat{u}_B\cdot\hat{r}_{AB})(\hat{u}_A\cdot\hat{u}_B)}{1-\chi'^2_{AB}(\hat{u}_A\cdot\hat{u}_B)^2}\right\}. \tag{A6}$$

The parameters χ'_{AB}, α'_{AB}, ν_{AB}, and μ_{AB} determine the potential energy as the rings approach with a given orientation. In this work, Prampolini's [81] rules for the evaluation of $\chi'_{AB}\alpha'^2_{AB}$, $\chi'_{AB}\alpha'^{-2}_{AB}$, and χ'^2_{AB} have been adopted

$$\chi'_{AB}\alpha'^2_{AB} = \frac{(\varepsilon^{ss}_{AA})^{1/\mu_{AA}}-(\varepsilon^{ee}_{AA})^{1/\mu_{AA}}}{(\varepsilon^{ss}_{AA})^{1/\mu_{AA}}+(\varepsilon^{ee}_{BB})^{1/\mu_{BB}}}, \tag{A7}$$

$$\chi'_{AB}\alpha'^{-2}_{AB} = \frac{(\varepsilon^{ss}_{BB})^{1/\mu_{BB}}-(\varepsilon^{ee}_{BB})^{1/\mu_{BB}}}{(\varepsilon^{ss}_{BB})^{1/\mu_{BB}}+(\varepsilon^{ee}_{AA})^{1/\mu_{AA}}}, \tag{A8}$$

$$\chi'^2_{AB} = \frac{[(\varepsilon^{ss}_{AA})^{1/\mu_{AA}}-(\varepsilon^{ee}_{AA})^{1/\mu_{AA}}][(\varepsilon^{ss}_{BB})^{1/\mu_{BB}}-(\varepsilon^{ee}_{BB})^{1/\mu_{BB}}]}{[(\varepsilon^{ss}_{BB})^{1/\mu_{BB}}+(\varepsilon^{ee}_{AA})^{1/\mu_{AA}}][(\varepsilon^{ss}_{AA})^{1/\mu_{AA}}+(\varepsilon^{ee}_{BB})^{1/\mu_{BB}}]}. \tag{A9}$$

---

[1] J. Dijon, in *Liquid Crystals: Applications and Uses*, edited by B. Bahadur (World Scientific, Singapore, 1990), Vol. 1.

[2] S. T. Lagerwall, in *Handbook of Liquid Crystals*, edited by D. Demus, J. W. Goodby, G. W. Gray, H. W. Spiess, and V. Vill (Wiley-VCH, Weinheim, 1998), Vol. 2B.

[3] S. J. Woltman, D. G. Jay, and P. G. Crawford, *Liquid Crystals: Frontiers in Biomedical Applications*, 1st ed. (World Scientific, Singapore, 2007).

[4] J. W. Goodby, R. Blinc, N. A. Clark, S. T. Lagerwall, M. A. Osipov, S. A. Pikin, T. Sakurai, K. Yoshino, and B. Zeks, *Ferroelectric Liquid Crystals: Principles, Properties, and Applications* (Gordon and Breach Science, Philadelphia, 1991).

[5] S. T. Lagerwall, *Ferroelectric and Antiferroelectric Liquid Crystals* (Wiley-VCH, Weinheim, 1999).

[6] R. Eelkema and B. L. Feringa, Org. Biomol. Chem. **4**, 3729 (2006).

[7] R. P. Lemieux, Acc. Chem. Res. **34**, 845 (2001).

[8] G. Proni and G. P. Spada, Enantiomer **6**, 171 (2001).

[9] M. A. Glaser, in *Advances in the Computer Simulations of Liquid Crystals*, edited by P. Pasini and C. Zannoni (Kluwer Academic, Dodrecht, 2000), Vol. 545, pp. 263–331.

[10] H. Stegemeyer, R. Meister, U. Hoffmann, A. Sprick, and A. Becker, J. Mater. Chem. **5**, 2183 (1995).

[11] M. J. Cook and M. R. Wilson, J. Chem. Phys. **112**, 1560 (2000).

[12] D. J. Earl and M. R. Wilson, J. Chem. Phys. **119**, 10280 (2003).

[13] D. J. Earl and M. R. Wilson, J. Chem. Phys. **120**, 9679 (2004).

[14] M. R. Wilson and D. J. Earl, J. Mater. Chem. **11**, 2672 (2001).

[15] C. J. Boulton, J. G. Finden, E. Yuh, J. J. Sutherland, M. D.

Wand, G. Wu, and R. P. Lemieux, J. Am. Chem. Soc. **127**, 13656 (2005).
[16] C. J. Boulton, J. J. Sutherland, and R. P. Lemieux, J. Mater. Chem. **13**, 644 (2003).
[17] C. S. Hartley, C. Lazar, M. D. Wand, and R. P. Lemieux, J. Am. Chem. Soc. **124**, 13513 (2002).
[18] C. S. Hartley and R. P. Lemieux, Liq. Cryst. **31**, 1101 (2004).
[19] C. S. Hartley, R. Y. Wang, and R. P. Lemieux, Chem. Mater. **16**, 5297 (2004).
[20] C. Lazar, K. X. Yang, M. A. Glaser, M. D. Wand, and R. P. Lemieux, J. Mater. Chem. **12**, 586 (2002).
[21] D. Vizitiu, C. Lazar, B. J. Halden, and R. P. Lemieux, J. Am. Chem. Soc. **121**, 8229 (1999).
[22] C. S. Hartley, N. Kapernaum, J. C. Roberts, F. Giesselmann, and R. P. Lemieux, J. Mater. Chem. **16**, 2329 (2006).
[23] T. Hegmann and R. P. Lemieux, J. Mater. Chem. **12**, 3368 (2002).
[24] T. Hegmann, M. R. Meadows, M. D. Wand, and R. P. Lemieux, J. Mater. Chem. **14**, 185 (2004).
[25] E. de Miguel and E. M. del Rio, Phys. Rev. Lett. **95**, 217802 (2005).
[26] J. A. Capitan, Y. Martinez-Raton, and J. A. Cuesta, J. Chem. Phys. **128**, 194901 (2008).
[27] C. Avendaño, A. Gil-Villagas, and E. González-Tovar, J. Chem. Phys. **128**, 044506 (2008).
[28] A. Cuetos and B. Martinez-Haya, J. Chem. Phys. **129**, 214706 (2008).
[29] P. J. Camp, M. P. Allen, and A. J. Masters, J. Chem. Phys. **111**, 9871 (1999).
[30] Y. Lansac, P. K. Maiti, N. A. Clark, and M. A. Glaser, Phys. Rev. E **67**, 011703 (2003).
[31] M. P. Neal and A. J. Parker, Chem. Phys. Lett. **294**, 277 (1998).
[32] C. Zannoni, J. Mater. Chem. **11**, 2637 (2001).
[33] M. O. Sinnokrot and C. D. Sherrill, J. Phys. Chem. A **108**, 10200 (2004).
[34] M. O. Sinnokrot and C. D. Sherrill, J. Phys. Chem. A **110**, 10656 (2006).
[35] M. J. T. Frisch *et al. Gaussian 03 Revision C.02* (Gaussian, Inc., Wallingford, CT, 2004).
[36] A. D. Becke, J. Chem. Phys. **98**, 5648 (1993).
[37] T. Clark, J. Chandrasekhar, G. W. Spitznagel, and P. V. Schleyer, J. Comput. Chem. **4**, 294 (1983).
[38] M. J. Frisch, J. A. Pople, and J. S. Binkley, J. Chem. Phys. **80**, 3265 (1984).
[39] C. M. Breneman and K. B. Wiberg, J. Comput. Chem. **11**, 361 (1990).
[40] See supplementary material at http://link.aps.org/supplemental/10.1103/PhysRevE.81.041704 for full details of the 2PhP and 5PhP molecular models including atomic charges, Lennard-Jones parameters, and intramolecular potential parameters.
[41] H. C. Andersen, J. Comput. Phys. **52**, 24 (1983).
[42] J. P. Ryckaert and A. Bellemans, Chem. Phys. Lett. **30**, 123 (1975).
[43] I. Cacelli, G. Cinacchi, C. Geloni, G. Prampolini, and A. Tani, Mol. Cryst. Liq. Cryst. **395**, 171 (2003).
[44] G. La Penna, D. Catalano, and C. A. Veracini, J. Chem. Phys. **105**, 7097 (1996).
[45] C. McBride and M. R. Wilson, Mol. Phys. **97**, 511 (1999).
[46] C. W. Cross and B. M. Fung, J. Chem. Phys. **101**, 6839 (1994).
[47] I. Cacelli, G. Cinacchi, G. Prampolini, and A. Tani, J. Am. Chem. Soc. **126**, 14278 (2004).
[48] I. Cacelli, G. Cinacchi, G. Prampolini, and A. Tani, J. Chem. Phys. **120**, 3648 (2004).
[49] M. A. Bates and G. R. Luckhurst, J. Chem. Phys. **110**, 7087 (1999).
[50] E. Bartsch, H. Bertagnolli, and P. Chieux, Ber. Bunsenges. Phys. Chem. **90**, 34 (1986).
[51] E. Bartsch, H. Bertagnolli, G. Schultz, and P. Chieux, Ber. Bunsenges. Phys. Chem. **89**, 147 (1985).
[52] R. Felici, F. Cilloco, and P. Bosi, Mol. Phys. **70**, 455 (1990).
[53] M. Misawa and T. Fukunaga, J. Chem. Phys. **93**, 3495 (1990).
[54] A. H. Narten, J. Chem. Phys. **67**, 2102 (1977).
[55] M. I. Cabaço, Y. Danten, M. Besnard, Y. Guissani, and B. Guillot, J. Phys. Chem. B **101**, 6977 (1997).
[56] R. Chelli, G. Cardini, P. Procacci, R. Righini, S. Califano, and A. Albrecht, J. Chem. Phys. **113**, 6851 (2000).
[57] J. H. Kim and S. H. Lee, Bull. Korean Chem. Soc. **23**, 441 (2002).
[58] J. H. Kim and S. H. Lee, Bull. Korean Chem. Soc. **23**, 447 (2002).
[59] M. R. Battaglia, A. D. Buckingham, and J. H. Williams, Chem. Phys. Lett. **78**, 421 (1981).
[60] D. R. Falcone, D. C. Douglass, and D. W. Mccall, J. Phys. Chem. **71**, 2754 (1967).
[61] K. Graupner and E. R. S. Winter, J. Chem. Soc. 1952, 1145.
[62] H. Hiraoka, J. Osuji, and W. Jono, Rev. Phys. Chem. Jpn. **28**, 52 (1958).
[63] R. E. Rathbun and A. L. Babb, J. Phys. Chem. **65**, 1072 (1961).
[64] I. Cacelli and G. Prampolini, J. Phys. Chem. A **107**, 8665 (2003).
[65] G. H. Tao and R. M. Stratt, J. Phys. Chem. B **110**, 976 (2006).
[66] J. Červená, R. Bayer, and W. Schäferlingová, Czech. J. Phys., Sect. B **23**, 1187 (1973).
[67] M. P. Allen and D. J. Tildesley, *Computer Simulation of Liquids* (Oxford University Press, New York, 1994).
[68] G. Ayton, D. Q. Wei, and G. N. Patey, Phys. Rev. E **55**, 447 (1997).
[69] E. D. Cressman, J. Dunford, R. Pecheanu, Y. Huh, S. Nita, I. Paci, S. Wang, C. Zhao, and N. M. Cann (unpublished).
[70] H. C. Andersen, J. Chem. Phys. **72**, 2384 (1980).
[71] G. J. Martyna, D. J. Tobias, and M. L. Klein, J. Chem. Phys. **101**, 4177 (1994).
[72] M. Parrinello and A. Rahman, Phys. Rev. Lett. **45**, 1196 (1980).
[73] W. G. Hoover, Phys. Rev. A **31**, 1695 (1985).
[74] W. G. Hoover, Phys. Rev. A **34**, 2499 (1986).
[75] S. Nosé, Mol. Phys. **52**, 255 (1984).
[76] S. Nosé, J. Chem. Phys. **81**, 511 (1984).
[77] S. Nosé and M. L. Klein, Mol. Phys. **50**, 1055 (1983).
[78] A. J. McDonald and S. Hanna, J. Chem. Phys. **124**, 164906 (2006).
[79] R. Berardi, A. P. J. Emerson, and C. Zannoni, J. Chem. Soc., Faraday Trans. **89**, 4069 (1993).
[80] D. J. Cleaver, C. M. Care, M. P. Allen, and M. P. Neal, Phys. Rev. E **54**, 559 (1996).
[81] G. Prampolini, J. Chem. Theory Comput. **2**, 556 (2006).